npj computational materials

www.nature.com/npjcompumats

ARTICLE OPEN

Check for updates

Remote substituent effects on catalytic activity of metal-organic frameworks: a linker orbital energy model

Zhenzhen Wang[1], Huan Meng[2], Xuejiao J. Gao[3], Jia-Jia Zheng[1] and Xingfa Gao[1]✉

The Hammett equation is commonly used to theoretically depict the remote electronic effects of substituents on catalytic activities of metal nodes of metal-organic frameworks (MOFs). However, the application of the theory to MOF catalysts usually encounters problems because it relies heavily on empirical parameters with unknown transferability. To develop an alternative prediction theory, the linker orbital energy model has been proposed by density functional theory calculations. The model provides a simple method to approximately depict the remote electronic substituent effects on catalytic activities of metal nodes of MOFs, and its general applicability to MOFs is supported by extensively revisiting the structure-activity relationships reported in the literatures. The model can be used to design catalytic activity of metal nodes of MOFs by engineering the electronic properties of linkers and substituents.

npj Computational Materials (2023)9:59 ; https://doi.org/10.1038/s41524-023-01008-5

INTRODUCTION

The coordination interaction of metal atoms with aryl ligands constitutes a wide variety of catalysts in the world, which range from heme enzymes[1] to various organic-inorganic hybrid catalytic materials[2–5]. The knowledge how aryl ligands regulate the catalytic activities of metal atoms linked to them is thus of great importance to both fundamental chemistry and catalytic applications of such metal-aryl hybrids, which, however, is still an elusive question[6].

The insufficient knowledge of how aryl ligands alter the catalytic activities of metal atoms is recently particularly reflected in the study of the catalytic functions of metal-organic frameworks (MOFs). MOFs refer to a family of porous crystalline materials formed by interconnecting metal nodes and organic linkers (Fig. 1a)[7–9]. Their potentials as engineered catalytic materials have recently attracted much interest[10–15]. Ideally, the metal nodes can serve as the active sites to catalyze chemical reactions if they contain coordinatively unsaturated metals and the linker substituents as the control factors to further fine-tune the catalytic activities of the metal nodes[16]. However, the practical implementation of this idea usually encounters unpredictable outcomes when attempting to tune the activities by varying linker substituents, because of the lack of a simple guiding theory for the effects of linker substituents on the catalytic activities.

So far, Hammett substituent constant (σ)[17,18] and its extensions[19–21] are the commonly-used methods to quantitatively describe the electronic effects of linker substituents on catalytic activities of metal nodes of MOFs. As early as 1937, Hammett[18] revealed the following linear relationship between the rate constant of the dissociation of benzoic acid (k_0) and those of the dissociations of its substituted derivatives (k):

$$\lg\frac{k}{k_0} = \rho\sigma \quad (1)$$

In Eq. (1), σ is the substituent constant depending on the nature of substituent; ρ is the constant depending on reaction environment and mechanism. Because the σ constants correlate closely with the well-known concepts—electron-donating and withdrawing abilities of the substituents, they been widely applied to quantitatively depict the relationships between the structures and reactivities of substituted organic compounds[22–29].

Indeed, Hammett σ constants have been successfully used to depict the linker substituent effects on thermal catalytic activities of several MOFs[30–33]. Shown in Fig. 1b is the MOF named UiO-66-X[30]. They are formed by zirconium cluster $Zr_6(\mu\text{-}O)_4(\mu\text{-}OH)_4$ and the X-substituted linker called benzene-1,4-dicarboxylic acid (BDC). They have been regarded the prototypes of MOFs to study the linker substituent effects. Vermoortele *et al.* have reported that the activities of UiO-66-X in catalyzing the cyclization of citronellal to isopulegol, which is denoted as Reaction 1 hereafter, exhibit a positive relationship with the σ constants of substituents X (Fig. 1c)[31]. Likewise, Hammett σ constants have successfully explained the substituent effects for the oxidase-mimicking catalysis of MIL-53(Fe)[32] and some other Lewis acid catalysis of MIL-101(Cr)[33].

However, the limitations of Hammett σ constant are also obvious. (1) Because it is obtained for substituents based on the thermodynamics of specific reactions, the transferability of the constant to other reactions is unknown. Although extensions like σ^+, σ^-, and $\sigma_{Pd}{}^+$ have been derived to adapt to other reactions[19–21], the simplicity and universality of the method are reduced. (2) Because it is devised for only substituent effects, the constant is not applicable to reactions in which the linkers also vary. Also shown in Fig. 1b are UiO-67-*o*-X and UiO-67-*m*-X. Unlike UiO-66-X, these MOFs are formed by the zirconium cluster and the linker called X-substituted biphenyl-4,4′-dicarboxylic acid (BPDC). Recently, Farha et al. have reported that UiO-66-X, UiO-67-*o*-X, and UiO-67-*m*-X can all catalyze the hydrolysis of dimethyl 4-nitrophenyl phosphonate (DMNP), denoted as Reaction 2 hereafter (Fig. 1c)[34–36]. Because of the limitations, Hammett σ constant is not applicable to such MOFs with varying linkers (BDC and BPDC). It is desirable to study the mechanism of the substituent effects and develop a more general prediction model.

[1]Laboratory of Theoretical and Computational Nanoscience, National Center for Nanoscience and Technology of China, Beijing, China. [2]CAS Key Laboratory for Biomedical Effects of Nanomaterials and Nanosafety, National Center for Nanoscience and Technology of China, Beijing, China. [3]College of Chemistry and Chemical Engineering, Jiangxi Normal University, Nanchang, China. ✉email: gaoxf@nanoctr.cn

In this work, the full pathways for UiO-66-X MOFs to catalyze Reactions 1 and 2 will be investigated by density functional theory (DFT) calculations and using the cluster models of MOFs. The result will suggest the underlying mechanism for the substituent effects on the catalytic activities. The approximately linear relationships between the key energy barriers of the catalyses and the linker orbital energies of the MOFs will be established. Such linear relationships will suggest linker orbital energy to be the effective descriptor for the remote substituent effects on the catalytic activities. With linker orbital energy as the descriptor, the linker orbital energy model, which approximately describes the substituent effects on catalytic activities of metal nodes of MOFs, will be developed and verified. The linker orbital model does not rely on empirical parameters, and it is applicable to MOFs with varying linkers and substituents. It may serve as a more general prediction model than Hammett, which can be used to design catalytic activity of metal nodes of MOFs by engineering the electronic properties of linkers and substituents.

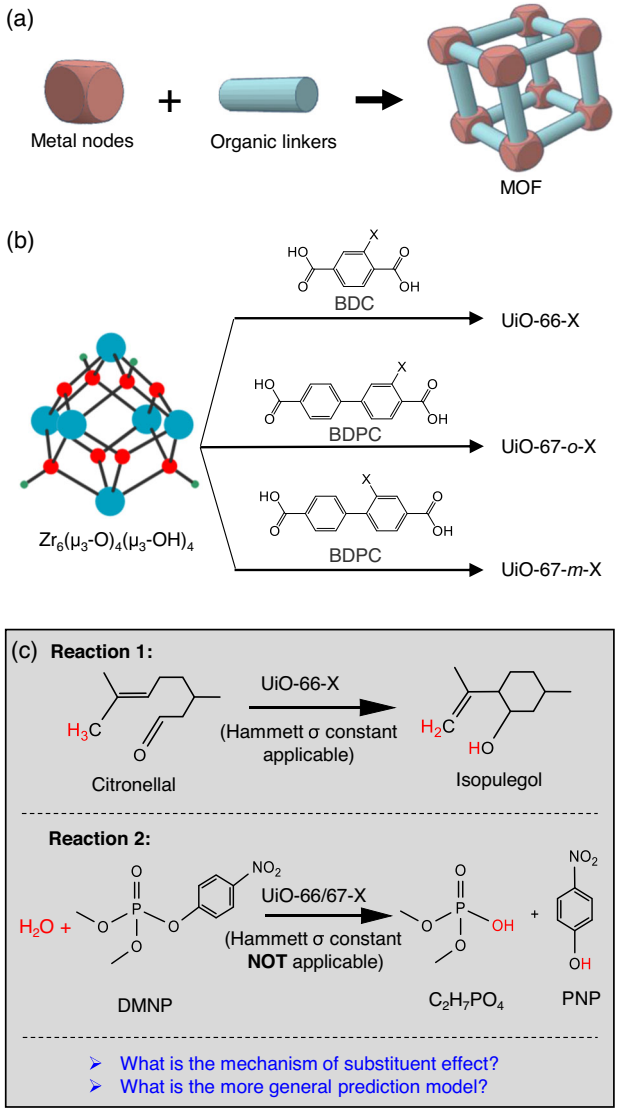

Fig. 1 Metal-organic frameworks (MOFs) and reactions catalyzed by them. a Construction of a MOF structure with the metal nodes and organic linkers; **b** Construction of the UiO-66-X, UiO-67-*o*-X, and UiO-67-*m*-X MOFs, in which X-substituted benzene-1,4-dicarboxylic acid (BDC) and biphenyl-4,4′-dicarboxylic acid (BPDC) are the linkers. **c** Reactions 1 and 2 catalyzed by the MOFs and the questions to be studied in this work. In **c**, the atoms closely relevant to the reactions are shown in red. The color setting for atoms in **b**: Zr, gray blue; H, green; O, red; C, gray.

RESULTS

Electronic substituent effects on the energy barriers

To study electronic substituent effects on the key catalytic energy barriers of Reactions 1 and 2, the mechanisms and kinetics of both reactions catalyzed by UiO-66-X (X = H, NH_2, and NO_2) were comparatively studied using DFT calculations based on Structure-A and B (Fig. 2a). The details of the calculations are given in the Method section. According to the calculations, Reaction 1 catalyzed by Structure-A (X = H, NH_2, and NO_2) all follow the mechanism of Fig. 3a. Namely, the transfer of H atom from the

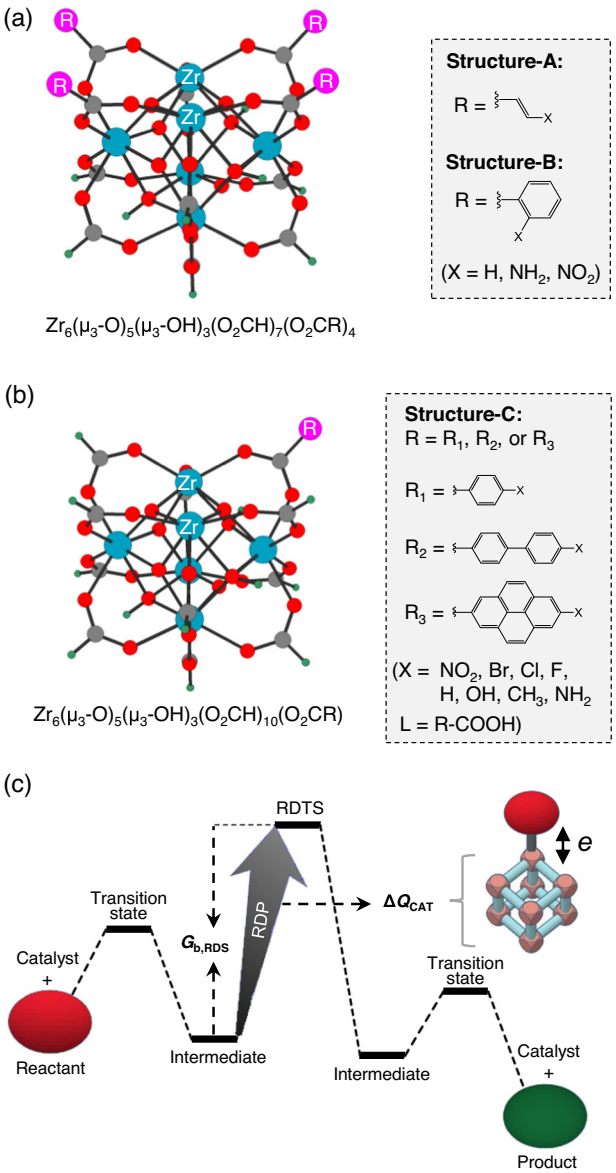

Fig. 2 Structural models of UiO-66 and the definition of quantities relevant to the catalytic kinetics. a Structure-A and B. **b** Structure-C. **c** Diagram showing definitions of rate-determining transition state (RDTS), rate-determining process (RDP), free energy barrier for rate-determining step ($G_{b,RDS}$), and change of catalyst charge in RDP (ΔQ_{CAT}). In **a**, **b**, the coordinatively unsaturated zirconium atoms are labeled, and the color setting for atoms is: Zr, gray blue; H, sea green; O, red; C, gray; R, pink.

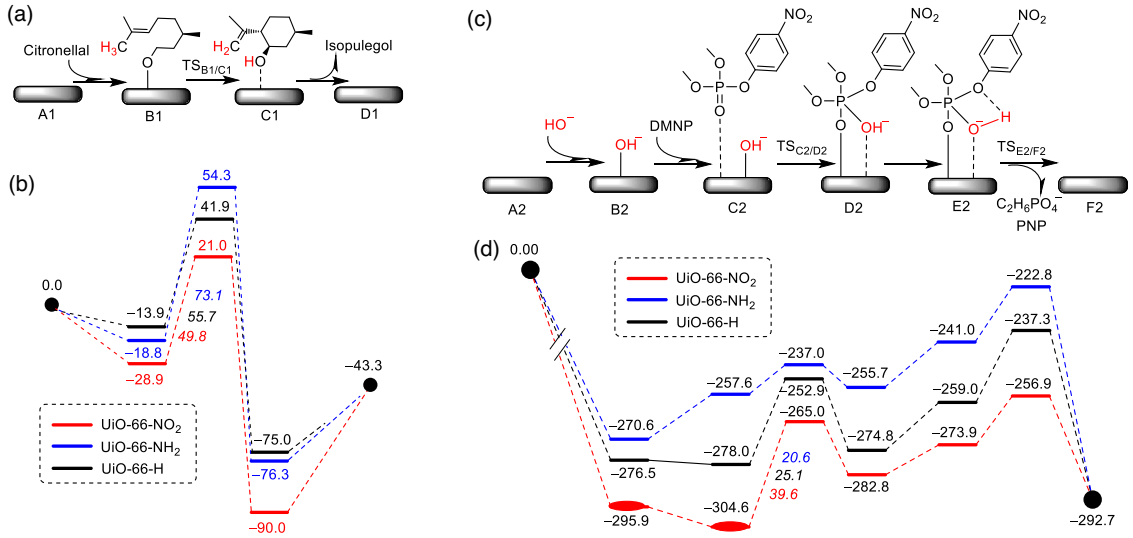

Fig. 3 Mechanisms and kinetics of the UiO-66-X catalyzed reactions obtained by DFT calculations. a, **b** Mechanisms and corresponding free energy profiles for Reactions 1. **c**, **d** Mechanisms and corresponding free energy profiles for Reactions 2. In **b**, **d**, relative free energies are labelled; free energy barriers of the rate-determining steps are shown in italic (energy unit: kJ mol^{-1}).

carbon to oxygen and the formation of the carbon-carbon bond proceed in a concerted manner, converting the citronellal to isopulegol (B1 → C1). The reaction energy profiles for this mechanism are shown in Fig. 3b. This mechanism is consistent with that obtained by DFT calculations using Structure-B (X = H, NH_2, and NO_2) by us (Supplementary Fig. 1). It is also consistent with that obtained using the similar method (X = H and NO_2) by Vermoortele et al. [31]. The kinetically less favorable pathways are shown in Supplementary Fig. 2. The Gibbs free energy barriers ($G_{b,RDS}$'s) of the rate determining steps (RDS) for substituents NH_2, H, and NO_2, are 73.1, 55.7, and 49.8 kJ mol^{-1}, respectively. These $G_{b,RDS}$ results match well with the experimentally observed increasing activity order UiO-66-NH_2 < UiO-66-H < UiO-66-NO_2 [31].

As for Reaction 2, the catalyses by Structure-A (X = H, NH_2, and NO_2) all follow the mechanism of Fig. 3c. Because Reaction 2 experimentally occurred in a basic condition with pH = 10, both hydroxyl anion OH^- and H_2O were considered as the hydrolysis agents. The pathway of OH^- has a lower $G_{b,RDS}$ and thus is discussed here. The hydrolysis mainly consists of three steps: First, the consecutive adsorption of OH^- and DMNP on the catalyst surface (A2 → B2 → C2); second, the transfer of OH adsorbate from the catalyst to the phosphorus center of DMNP to form the five-coordinated phosphorus intermediate, following by the conformational change to form the hydrolysis-ready intermediate (C2 → D2 → E2); third, the intramolecular hydrogen transfer yielding the products (E2 → F2). The corresponding free energy profiles are shown in Fig. 3d. For each of the three catalysts, C2 → D2, namely, the transfer of the OH adsorbate from MOF to the DMNP has the highest free energy barrier, corresponding to the RDS. The $G_{b,RDS}$'s for UiO-66-NH_2, UiO-66-H, and UiO-66-NO_2 are 20.6, 25.1, and 39.6 kJ mol^{-1}, respectively, in good agreement with the experimentally observed decreasing activity, UiO-66-NH_2 > UiO-66-H > UiO-66-NO_2 [34–36]. The kinetically less favorable pathways are shown in Supplementary Fig. 3. Similar mechanisms have been previously reported for the hydrolysis of sarin[37] and organophosphate warfare agents[11,38].

The above results suggest that Reactions 1 and 2 catalyzed by the UiO-66-X MOFs have an opposite linker-substituent effects on the catalytic activities, which agree well the structure-activity relationships of both reactions experimentally reported before[31,34]. The consistency between the computed $G_{b,RDS}$ and experimental activity orders confirms that the cluster models of UiO-66-X used in this work is suitable for studying the electronic substituent effects.

Mechanism of the electronic substituent effects

To study the underlying mechanism for the opposite electronic substituent effects, charge population analysis was performed for structures involved in the RDSs for both reactions. To be different from RDS, structural conversion from the previously neighboring intermediate to the rate-determining transition state (RDTS) in the reaction path is denoted as the rate-determining process (RDP) hereafter. Furthermore, the total number of charge located on the catalyst region, which includes the metal node and organic linkers, of the catalyst-reactant complex is denoted as (Q_{CAT}), and the variation of Q_{CAT} in the RDP is denoted as ΔQ_{CAT} hereafter (Fig. 2c). The RDS of Reaction 1 is B1 → $TS_{B1/C1}$ → C1. Intermediates B1 and C1 and transition state $TS_{B1/C1}$ are shown in Fig. 4a, in which the Q_{CAT} values are marked. As can be seen, although Q_{CAT} increases from −0.241 in B1 to −0.217 in C1, it decreases from −0.241 in B1 to −0.287 in $TS_{B1/C1}$. Therefore, $\Delta Q_{CAT} = -0.046$ (Fig. 4a). To obtain detailed charge-evolution information, intrinsic reaction coordinate (IRC) calculation was performed to locate transient structures linking the stationary points, and then charge population analysis was performed for these transient structures. The results are plotted in Fig. 4b, which verify that the RDP is featured by electron transfer from the reactant to the catalyst moiety ($\Delta Q_{CAT} < 0$). Because an electron-withdrawing substituent enhances the ability of MOFs to accept electrons, substituent like NO_2 reduces the $G_{b,RDS}$ and improves the catalytic activity. On the contrary, because an electron-donating substituent decreases the ability of MOFs to accept electrons, substituent like NH_2 increases the $G_{b,RDS}$ and reduces the catalytic activity. The above results profoundly explain the mechanism for the activity order of Reaction 1: UiO-66-NH_2 < UiO-66-H < UiO-66-NO_2 [31].

As for Reaction 2, the RDS is C2 → $TS_{C2/D2}$ → D2. Shown in Fig. 4c are intermediates C2 and D2 and transition state $TS_{C2/D2}$. The Q_{CAT} increases from 0.325 in C2 to 0.420 in $TS_{C2/D2}$ ($\Delta Q_{CAT} = 0.095$) and further increases to 0.515 in D2, suggesting that electrons are transferred from the catalyst to the reactant moiety in the RDP. This charge population result is further evidenced by the result of Fig. 4d, which shows the detailed charge evolution along the IRC. Because an electron-donating substituent enhances the ability of MOFs to transfer electrons away, the result profoundly explains

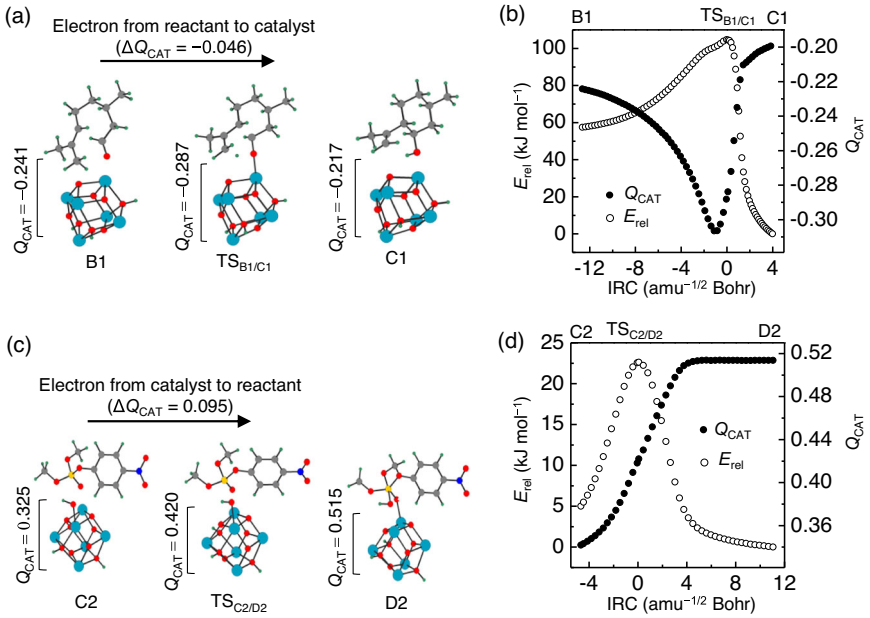

Fig. 4 Variation of catalyst charge in rate-determining steps. a, **c** Catalyst charge variation (ΔQ_{CAT}) for structures involved in the rate-determining steps of Reactions 1 and 2, respectively. **b**, **d** Variation of total energy (E_{rel}) and ΔQ_{CAT} with intrinsic reaction coordinate (IRC) for Reactions 1 and 2, respectively. For structures in (**a**, **c**), the linkers are not shown for clarity. The color setting for atoms in **a**, **c**: Zr gray blue, H sea green, O red, C gray, N blue; P, gold.

the mechanism for the activity order of Reaction 2: UiO-66-NH_2 > UiO-66-H > UiO-66-NO_2[34].

Taken together, the mechanism for the electronic substituent effects on the catalytic activities of metal nodes of MOFs can be ascribed to ΔQ_{CAT}, namely, the variation of catalyst charge in the RDP. In case of $\Delta Q_{CAT} < 0$ (e.g., Reaction 1), the activity is closely relevant to the electron transfer from the reactant to catalyst moiety in the RDP. Because electron withdrawing substituents are beneficial to such an electron transfer, they will reduce $G_{b,RDS}$ and increase the catalytic activity. In case of $\Delta Q_{CAT} > 0$ (e.g., Reaction 2), the activity is closely relevant to the electron transfer from the catalyst to reactant moiety in the RDP. Because electron donating substituents are beneficial to such an electron transfer, they will reduce $G_{b,RDS}$ and increase the catalytic activity. The above result profoundly explains the opposite electronic substituent effects of UiO-66-X in catalyzing Reactions 1 and 2[31,34].

Linker orbital energy model

To quantitatively describe the electronic substituent effects on thermal catalytic activity of metal nodes of UiO-66-X MOFs, the linker orbital energy model was established. To this end, the orbital interaction between reactant and catalyst moieties was analyzed for $TS_{B1/C1}$ and $TS_{C2/D2}$, i.e., the RDTS for Reactions 1 and 2, using the ETS-NOCV method[39]. The results are present in Fig. 5a and Supplementary Fig. 4. As can be seen, the main orbital interactions of both RDTSs are similar, which is the interaction between the metal d_{z^2} orbital and linker p orbital. Owing to the remote π-d conjugation between the linker substituent and nodal metal, the substituent will tune the extranuclear electron density and consequently effective nuclear charge (Z_{eff}) of the metals (Fig. 5b and Supplementary Fig. 5). This will further tune the catalytic activity of the metal by tuning the energies of molecular orbitals, including the d_{z^2} orbital, localized on it. Such substituent effect on catalytic activity via the π-d conjugation is sometimes understood by that the remote conjugation tunes the Lewis acidities of the nodal metals[31,33,40].

To establish a quantitative relationship between the catalytic activity (estimated by value of $G_{b,RDS}$) and orbital energy, the frontier orbital energies of substituted catalysts and $G_{b,RDS}$'s were calculated for Reactions 1 and 2, using Structure-C (R = R_1; X = NH_2, CH_3, OH, H, F, Cl, Br, NO_2, CHO, CN, CF_3) as the model of UiO-66-X (Fig. 2b). The reason of using Structure-C is discussed in the Method section. The $G_{b,RDS}$ of Reaction 1 scales positively with the LUMO energies of the catalyst, $E_{CAT,LUMO}$ (Fig. 5c); likewise, the $G_{b,RDS}$ of Reaction 2 scales negatively with the $E_{CAT,LUMO}$ (Fig. 5d). Different equations like linear and exponential functions were used to fit $G_{b,RDS}$ with $E_{CAT,LUMO}$. For simplicity and avoiding overfitting, the linear relationships were adopted here for further discussion (for exponential fitting, see Supplementary Fig. 6). For both reactions, the $G_{b,RDS}$ also shows the scaling relationships with the corresponding HOMO energy of the catalyst ($E_{CAT,HOMO}$), but the R^2 fitted with $E_{CAT,HOMO}$ are smaller than the corresponding R^2 with $E_{CAT,LUMO}$ (Supplementary Fig. 7). The better relationship of $G_{b,RDS}$ with $E_{CAT,LUMO}$ may be ascribed to that the metal d_{z^2} orbital constitutes the main orbital interaction in the RDTS, as suggested by Fig. 5a.

Interestingly, the frontier orbital energies of the catalysts have good linear relationships with the corresponding frontier orbital energies of the linkers: the LUMO of linker ($E_{L,LUMO}$) scales linearly with $E_{CAT,LUMO}$ with $R^2 = 0.99$ for the linear fitting (Fig. 5e); the HOMO of linker ($E_{L,HOMO}$) scales linearly with $E_{CAT,HOMO}$ with $R^2 = 0.97$ (Fig. 5f). Such good linearly relationships can be ascribed to that both HOMO and LUMO of the UiO-66-X clusters are mainly located on the linkers (Supplementary Fig. 8). Based on the approximately linear relationships between $G_{b,RDS}$ and E_{LUMO}, the following equation can be derived:

$$\ln\left(\frac{r_{MOF-X}}{r_{MOF-H}}\right) = m\Delta Q_{CAT}E_{L,LUMO} + n \quad (2)$$

The details of the derivation of Eq. (2) can be found in the Supplementary Note 1. In Eq. (2), r_{MOF-X} and r_{MOF-H} mean the catalytic reaction rates of substituted and unsubstituted MOFs, respectively; m and n are constants depending on the catalytic system and $m > 0$. Equation (2) quantitatively describes the remote electronic effects of substituents on catalytic activity of metal nodes of MOFs. Especially, the slope of the linear function of

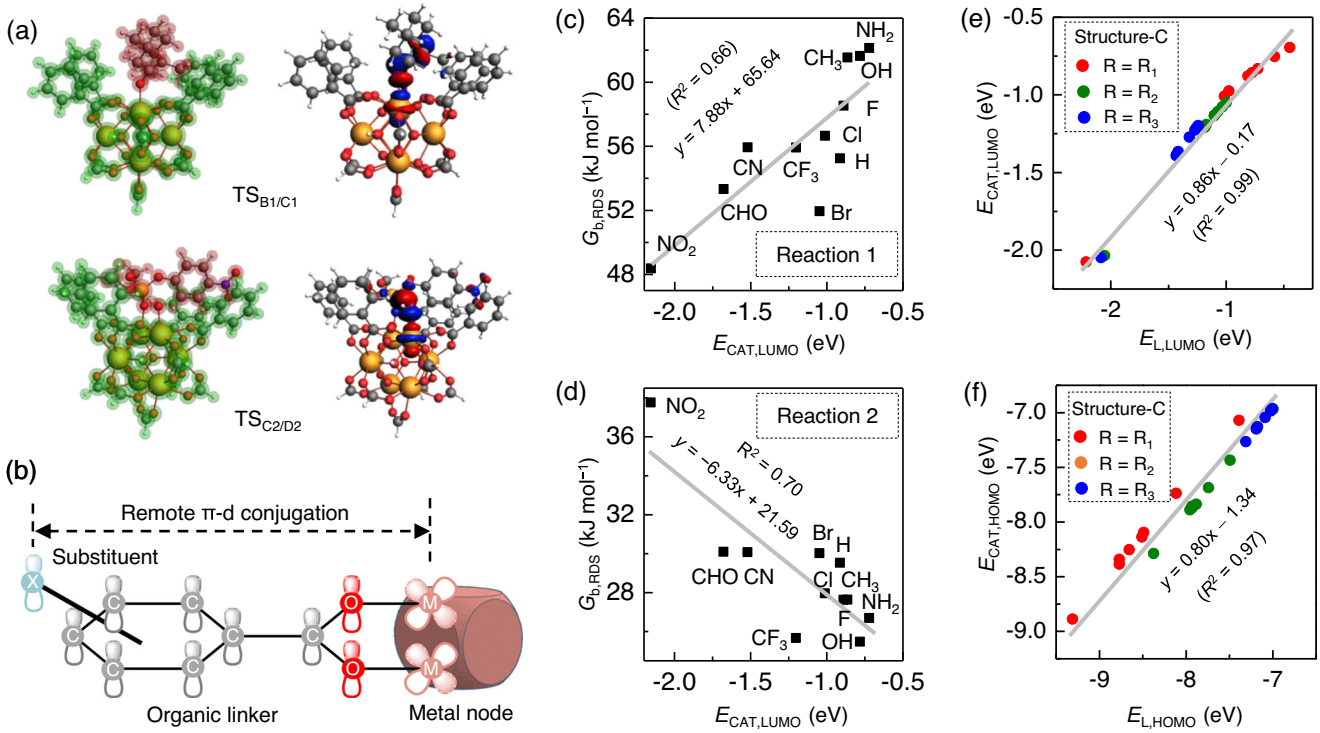

Fig. 5 Relationships between energy barriers and linker frontier orbital energies. a Orbital interaction analysis for rate-determining transition states. **b** Remote π-d conjugation between the linker substituent and nodal metal. **c** Plot of free energy barriers of the rate-determining step ($G_{b,RDS}$) with catalyst LUMO energies ($E_{CAT,LUMO}$) for Reaction 1. **d** Plot of $G_{b,RDS}$ with catalyst LUMO energies ($E_{CAT,LUMO}$) for Reaction 2. **e** Plot of $E_{CAT,LUMO}$ with linker LUMO energy ($E_{L,LUMO}$). **f** Plot of $E_{CAT,HOMO}$ with linker HOMO energy ($E_{L,HOMO}$). The color setting for atoms in **a**, **b**: Zr, yellow; H, white; O, red; C, gray.

Eq. (2) indicates the plus or minus sign of ΔQ_{CAT}, providing mechanistic insights into the catalytic mechanisms.

Comparing Eq. (1) and Eq. (2), it is obvious that item $m\Delta Q_{CAT}$ of Eq. (2) corresponds to ρ of Equation (2), and $E_{L,LUMO}$ of Eq. (2) corresponds to σ of Eq. (1). This suggests that Hammett constant should have linear relationship with $E_{L,LUMO}$. The plots of σ and its extensions with $E_{L,LUMO}$ are present in Supplementary Fig. 9 and Table 1, in which the approximate linear relationships of the constants with $E_{L,LUMO}$ can indeed be found. This result confirms the potential of $E_{L,LUMO}$ as the activity descriptor of MOFs.

Noteworthily, although ΔQ_{CAT} is key to understanding the mechanisms underlying the model, the exact value of ΔQ_{CAT} is not required when using the linker orbital energy model. Similarly, the exact energies of ligand frontier orbitals with respect to vacuum energy, which are usually hard to obtain by DFT calculations, are also not required when using the model. Instead, obtaining the relative values of the orbital energies is sufficient for using the model. Because frontier orbital energies are intrinsic properties of linkers, whose relative values can be easily and reliably obtained by DFT calculations[41] or photoelectron spectroscopic experiments, the model provides a simple way to fine tuning catalytic activity of MOFs by engineering linker substituents.

Frontier orbital energies are intrinsic electronic properties of molecules closely relevant to chemical activities, on the basis of which a lot of activity principles have been successfully established for different scenarios before[42–45]. The present linker orbital energy model is devised for the electronic substituent effects on catalytic activities of metal nodes of MOFs. It is applicable to MOFs with the same metal nodes but similar linkers and different substituents, in which the linkers and substituents exert influences on the catalytic activity mainly through the electronic π-d conjugation rather than other effects like stereo-hindrance or hydrogen bonding. Such π-d conjugation usually exists in MOFs consisting of transition metals and aromatic linkers, in which the metals make bonds with the linker atoms through the hybridization involving the metal d and linker s and p orbitals (Supplementary Fig. 5). It is inapplicable to MOFs where the substituents are directly added to the metal nodes, not having the d-p π-conjugation[46]. It is also inapplicable to MOFs where metal nodes are not the catalytic active centers[47].

Experimental verification of the model

To verify its validity, the above linker orbital energy model has been used to revisit the structure-activity relationships of UiO-66 MOFs with a larger variety of linkers and substituents. For Reaction 1, UiO-66-X MOFs with eight substituents were considered (X = H, NH_2, OCH_3, F, CH_3, Br, Cl, NO_2); for Reaction 2, UiO-66-X (X = NH_2, NO_2, H), UiO-67-H, UiO-67-*m*-NH_2, and UiO-67-*o*-NH_2 were considered. The structure-activity relationships for these reactions have been experimentally studied before. The rates of Reaction 1 catalyzed by the UiO-66-X MOFs, which were taken from the study of Vermoortele et al.[31], are plotted in a linear function with the orbital energy $E_{L,LUMO}$ in Fig. 6a (for the source data, see Supplementary Table 2). The negative slope means $\Delta Q_{CAT} < 0$, which is in good agreement with the above result that the RDP of Reaction 1 has a minus ΔQ_{CAT}. Rates of Reaction 2[34] catalyzed by the UiO-66/67-X were taken from the study of Katz et al. and Islamoglu et al.[36]. As shown in Fig. 6b, they correlate in positively with $E_{L,LUMO}$, in good agreement with the above result that the RDP of Reaction 2 has a positive ΔQ_{CAT} ($\Delta Q_{CAT} > 0$). Therefore, the present results systematically disclose the underlying mechanisms for the previously reported linker and substituent effects on catalytic activities of UiO-66/67 MOFs.

To verify whether it is applicable to MOFs beyond UiO-66, the model has been further applied to revisit the structure-activity relationships for MIL-53(Fe)-X and MIL-101(Fe)-X MOFs, which catalytically activate O_2 to oxidize organic substrate as oxidases

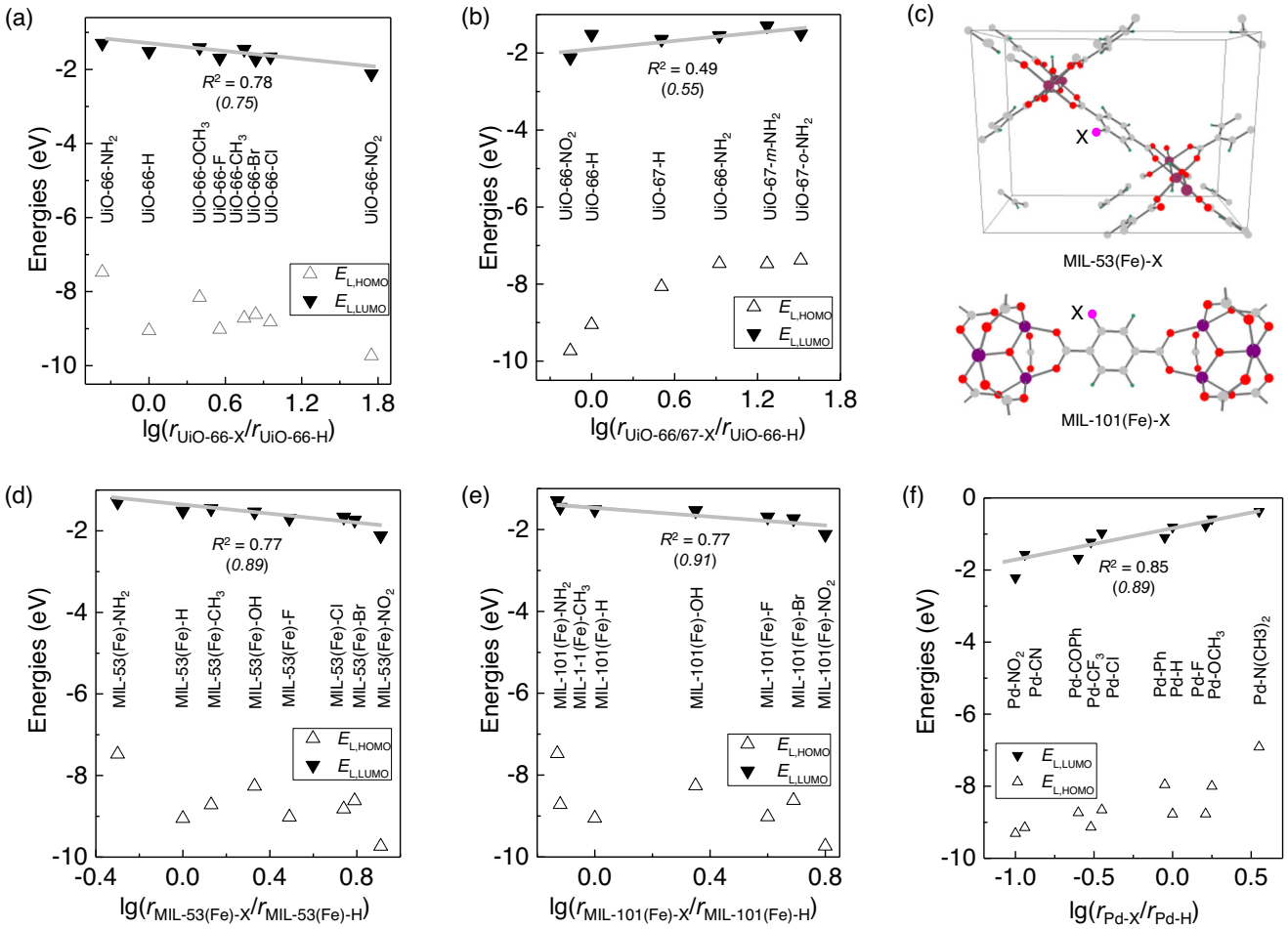

Fig. 6 Experimental verification of the prediction model. a, **b** Plots of $E_{L,LUMO}$ and $E_{L,HOMO}$ with the relative reaction rates of Reactions 1 and 2, respectively. **c** Partial structures of X-substituted MIL-53(Fe) and MIL-101(Fe) MOFs. **d**, **e** Plots of $E_{L,LUMO}$ and $E_{L,HOMO}$ with the relative reaction rates for the oxidase-like catalysis of MIL-53(Fe)-X and MIL-101(Fe)-X, respectively. **f** Plots of $E_{L,LUMO}$ and $E_{L,HOMO}$ with the relative reaction rates for ligand exchange of the palladium complex. In **a**, **b**, **d**-**f**, the solid lines are for eyesight guide.

do[32]. The structures of these two MOFs are shown in Fig. 6c. Wu et al. have reported that an electron-withdrawing substituents like NO_2 enhance the catalytic activities of both MOFs. Because an electron-withdrawing substituent reduces linker LUMO energies, it can be inferred from the model that the ΔQ_{CAT} of the catalyses have a minus sign ($\Delta Q_{CAT} < 0$). This mechanistic insight agrees well with the previous study that the RDS of the catalysis is indeed an electron-transfer-to-catalyst process[32]. Because $\Delta Q_{CAT} < 0$, it can be further inferred from the model that the relative catalytic activities of both MOFs correlate negatively with $E_{L,LUMO}$. As can be seen from Fig. 6d, e, the activities indeed scale negatively with $E_{L,LUMO}$. These results suggest that the linker orbital energy model is also applicable to MIL-53(Fe)-X and MIL-101(Fe)-X MOFs.

The model is even applicable to the substituent effects on activity of organometallic complexes beyond MOFs. Wu et al. have recently developed another substituent constant σ_{Pd}^{+}, which better describes the electronic effects of remote substituents on thermodynamics and kinetic of the palladium complexes[21]. The model was also used to revisit the activity of the ligand exchange reaction of the substituted palladium complexes. As shown in Fig. 6f, the relative rate of the ligand exchange reaction indeed has a linear relationship with the $E_{L,LUMO}$ of substituted benzoic acid, suggesting the general applicability of the model.

The above results also serve as the example applications of the model. Because Hammett theory[18] and its derivatives[21,22] have been widely used to quantify the electronic substituent effects on a large variety of materials properties, e.g., orbital energies[24], bonding energies[21,25], catalytic activity[26], reaction barriers[27], and reaction mechanisms[28,29], we expect that the present model will serves as the more simple and general theoretical tool for remote substituent effects on materials properties including catalytic activities of metal nodes of MOFs.

DISCUSSION

To summarize, the linker orbital energy model approximately describing the remote electronic effects of linker substituents on catalytic activities of metal nodes of MOFs has been developed and verified. The d_{z^2} orbital of nodal metals of MOFs, whose energy is crucially influenced by the remote substituent via the π-d conjugation, plays a vital role in the catalysis. The free energy barrier, $G_{b,RDS}$, of the rate-determining step of the catalysis scales approximately linearly with linker LUMO energy, $E_{L,LUMO}$, suggesting that $E_{L,LUMO}$ is the effective descriptor for the substituent effects on the catalytic activity. The plus or minus sign of the catalyst charge variation in the rate-determining process, namely ΔQ_{CAT}, signifies how $G_{b,RDS}$ depends on $E_{L,LUMO}$: $G_{b,RDS}$ scales positively with $E_{L,LUMO}$ if $\Delta Q_{CAT} < 0$; $G_{b,RDS}$ scales negatively with $E_{L,LUMO}$ if $\Delta Q_{CAT} > 0$. These results lead to the development of the model of Eq. (2), which quantitatively depicts the approximately linear relationship between the relative catalytic activities and $E_{L,LUMO}$. The validity of model has been supported by revisiting the

structure-activity relationships of different MOFs and reactions. The results profoundly explain the mechanisms for the previously reported linker and substituent effects on the catalytic activities of MOFs, which are the state-of-the-art questions of the research field. Compared to Hammett constants, the present model does not reply on empirical parameters, and it is applicable MOFs with not only varying substituents but varying linkers. The model may provide a general method to precisely design catalytic activity of metal nodes of MOFs by engineering the electronic properties of linkers and substituents.

METHODS

Structural models

The structures shown in Fig. 2 were used as the cluster models of UiO-66-X. Structure-A is composed by one metal node and four substituted vinyl groups, and Structure-B is composed by one metal node and four ortho-substituted phenyl groups (Fig. 2a). Cluster models rather than periodic slab models were used to represent UiO-66-X was for two reasons. First, all metal nodes in UiO-66-X are separated by aryl linkers and thus cluster models are sufficient to reproduce the local chemical environments of the metal nodes in UiO-66-X. Second, hybrid density functionals, which have been very successful in the field of computational chemistry[48], are extremely computationally demanding for the slab models. Indeed, Structure-B and similar cluster models have been successfully used as the models to study the catalytic mechanisms of UiO-66-X[31,36,49] and other MOFs before[16,50]. Our test calculations for Reaction 1 further suggested that catalytic mechanisms and activity orders, which were indicated by free energy barriers ($G_{b,RDS}$) of rate-determining steps (RDSs), calculated with Structure-A and Structure-B were identical (Supplementary Fig. 1). Compared to phenyl linkers of Structure-B, smaller vinyl linkers of Structure-A exert smaller steric hindrance to the reactions. Therefore, Structure-A is more suitable than Structure-B for studying electronic substituent effects of UiO-66-X, and was extensively used here to investigate the full catalytic mechanisms and energy changes.

Structure-C consisting of the metal node and only one aryl linker, was constructed as the simpler model of UiO-66-X (Fig. 2b). Using only one linker was intended to study the electronic effect of the specific linker. To focus on effects of linker orbital energies, the substituent in Structure-C was placed on the para- rather than ortho-position of the benzene ring to avoid the possible involvement of substituent steric effects. Structure-C is more concise than Structure-A and B and is more suitable for extensive calculations.

Calculations

All DFT calculations were performed in the solvent phase using the M062X density function[51]. The inexplicit solvent model, polarizable continuum model[52], was used to simulate the solvent effect. Toluene and water were selected as the solvent molecules for Reactions 1 and 2, respectively, according to the corresponding experimental studies[31,34,36]. All structures were obtained by locating geometries of stationary points in the potential energy surfaces. All intermediates and transition states on the potential energy surface were verified by checking the number of imaginary frequencies using frequency analysis calculations. The intermediate and transition state have zero and one imaginary frequency, respectively. The free energy data were also obtained through the frequency analysis calculations. The intrinsic reaction coordinates (IRCs) were obtained with the IRC method[53,54], and the charges were obtained using the natural population analysis (NPA) method[55]. All metal atoms were treated with the Lanl2DZ basis set and the Lanl2DZ effective core potential[56]. All nonmetal atoms were treated with the 6–31 G(d,p) or the 6–31 + G(d,p) basis set[57]. The 6–31 G(d,p) basis set was used to calculate the full catalytic mechanisms, free energy profiles, and the charge population analyses. The 6–31 + G(d,p) basis set with the "Grid=UltraFine" keyword was used to study the relationships of linker orbital energies with Hammett σ constants, the free energy barriers, and frontier orbital energies of catalysts. The above calculations were performed with the GAUSSIAN 09 program[58] with the default parameter setting if not mentioned otherwise. The reference of the orbital energies was the vacuum level by default.

The orbital interaction between reactant and catalyst moieties was analyzed using the extended transition state (ETS) method in conjunction with the natural orbitals for chemical valence (NOCV) theory[39]. The Becke−Perdew exchange-correlation functional BP86[59–61] with the TZ2P basis sets as implemented in the program package ADF2014.10. was used these calculations[62]. More details of this calculation method can be found in our previous study[63].

DATA AVAILABILITY

The authors declare that all other data supporting the findings of this study are available within the paper, the Supplementary Information file.

Received: 31 August 2022; Accepted: 26 March 2023;
Published online: 11 April 2023

REFERENCES

1. Poulos, T. L. Heme enzyme structure and function. *Chem. Rev.* **114**, 3919–3962 (2014).
2. Du, D.-Y., Qin, J.-S., Li, S.-L., Su, Z.-M. & Lan, Y.-Q. Recent advances in porous polyoxometalate-based metal–organic framework materials. *Chem. Soc. Rev.* **43**, 4615–4632 (2014).
3. Vilà-Nadal, L. & Cronin, L. Design and synthesis of polyoxometalate-framework materials from cluster precursors. *Nat. Rev. Mater.* **2**, 17054 (2017).
4. Goodman, E. D., Zhou, C. & Cargnello, M. Design of organic/inorganic hybrid catalysts for energy and environmental applications. *ACS Cent. Sci.* **6**, 1916–1937 (2020).
5. Lee, S., Jeong, H., Nam, D., Lah, M. S. & Choe, W. The rise of metal–organic polyhedra. *Chem. Soc. Rev.* **50**, 528–555 (2021).
6. Durand, D. J. & Fey, N. Computational ligand descriptors for catalyst design. *Chem. Rev.* **119**, 6561–6594 (2019).
7. Yaghi, O. M. et al. Reticular synthesis and the design of new materials. *Nature* **423**, 705–714 (2003).
8. Batten, S. R. et al. Coordination polymers, metal–organic frameworks and the need for terminology guidelines. *CrystEngComm* **14**, 3001–3004 (2012).
9. Furukawa, H., Cordova, K. E., O'Keeffe, M. & Yaghi, O. M. The chemistry and applications of metal-organic frameworks. *Science* **341**, 1230444 (2013).
10. Zhao, S.-N., Song, X.-Z., Song, S.-Y. & Zhang, H.-J. Highly efficient heterogeneous catalytic materials derived from metal-organic framework supports/precursors. *Coord. Chem. Rev.* **337**, 80–96 (2017).
11. Kirlikovali, K. O., Chen, Z., Islamoglu, T., Hupp, J. T. & Farha, O. K. Zirconium-based metal-organic frameworks for the catalytic hydrolysis of organophosphorus nerve agents. *ACS Appl. Mater. Interfaces* **12**, 14702–14720 (2020).
12. Liu, S. et al. Design of metal-organic framework-based photocatalysts for hydrogen generation. *Coord. Chem. Rev.* **413**, 213266 (2020).
13. Guo, J. et al. Metal–organic frameworks as catalytic selectivity regulators for organic transformations. *Chem. Soc. Rev.* **50**, 5366–5396 (2021).
14. Li, Y., Cui, M., Yin, Z., Chen, S. & Ma, T. Metal-organic framework based bifunctional oxygen electrocatalysts for rechargeable zinc-air batteries: current progress and prospects. *Chem. Sci.* **11**, 11646–11671 (2020).
15. Wang, Y. et al. Two-dimensional metal-organic frameworks with unique oriented Layers for oxygen reduction reaction: tailoring the activity through exposed crystal facets. *CCS Chem.* **4**, 1633–1642 (2022).
16. McCarver, G. A., Rajeshkumar, T. & Vogiatzis, K. D. Computational catalysis for metal-organic frameworks: an overview. *Coord. Chem. Rev.* **436**, 213777 (2021).
17. Hammett, L. P. Linear free energy relationships in rate and equilibrium phenomena. *Trans. Faraday Soc.* **34**, 156–165 (1938).
18. Hammett, L. P. The effect of structure upon the reactions of organic compounds. benzene derivatives. *J. Am. Chem. Soc.* **59**, 96–103 (1937).
19. Brown, H. C. & Okamoto, Y. Substituent constants for aromatic substitution. *J. Am. Chem. Soc.* **79**, 1913–1917 (1957).

20. Brown, H. C. & Okamoto, Y. Electrophilic substituent constants. *J. Am. Chem. Soc.* **80**, 4979–4987 (1958).
21. Wu, J.-Y., Mo, B.-R., Yang, J.-D. & Cheng, J.-P. A distinctive pattern for substituent effects on transition metal centers: enhanced electron-donating capacity of cationic palladium species. *CCS Chem*. https://doi.org/10.31635/ccschem.31022.202201990 (2022).
22. Hansch, C., Leo, A. & Taft, R. W. A survey of Hammett substituent constants and resonance and field parameters. *Chem. Rev.* **91**, 165–195 (1991).
23. Yadav, V. K. in *Steric and stereoelectronic effects in organic chemistry*, 179-189 (Springer International Publishing, Cham, 2021).
24. Chang, A. M., Freeze, J. G. & Batista, V. S. Hammett neural networks: prediction of frontier orbital energies of tungsten-benzylidyne photoredox complexes. *Chem. Sci.* **10**, 6844–6854 (2019).
25. Wu, J.-Y., Li, Z., Yang, J.-D. & Cheng, J.-P. Bonding energetics of palladium amido/aryloxide complexes in DMSO: implications for palladium-mediated aniline activation. *Angew. Chem. Int. Ed.* **59**, 23782–23790 (2020).
26. Kumar, G. et al. Evaluating differences in the active-site electronics of supported Au nanoparticle catalysts using Hammett and DFT studies. *Nat. Chem.* **10**, 268–274 (2018).
27. Bragato, M., von Rudorff, G. F. & von Lilienfeld, O. A. Data enhanced Hammett-equation: reaction barriers in chemical space. *Chem. Sci.* **11**, 11859–11868 (2020).
28. Cruz, C. L. & Nicewicz, D. A. Mechanistic investigations into the cation radical newman–kwart rearrangement. *ACS Catal.* **9**, 3926–3935 (2019).
29. Barbee, M. H. et al. Substituent effects and mechanism in a mechanochemical reaction. *J. Am. Chem. Soc.* **140**, 12746–12750 (2018).
30. Cavka, J. H. et al. A new zirconium inorganic building brick forming metal organic frameworks with exceptional stability. *J. Am. Chem. Soc.* **130**, 13850–13851 (2008).
31. Vermoortele, F. et al. Electronic effects of linker substitution on Lewis acid catalysis with metal-organic frameworks. *Angew. Chem. Int. Ed.* **51**, 4887–4890 (2012).
32. Wu, J. et al. Hammett relationship in oxidase-mimicking metal-organic frameworks revealed through a protein-engineering-inspired strategy. *Adv. Mater.* **33**, e2005024 (2021).
33. Santiago-Portillo, A., Navalón, S., Concepción, P., Álvaro, M. & García, H. Influence of terephthalic acid substituents on the catalytic activity of MIL-101(Cr) in three lewis acid catalyzed reactions. *ChemCatChem* **9**, 2506–2511 (2017).
34. Katz, M. J. et al. Exploiting parameter space in MOFs: a 20-fold enhancement of phosphate-ester hydrolysis with UiO-66-NH_2. *Chem. Sci.* **6**, 2286–2291 (2015).
35. Katz, M. J. et al. One step backward is two steps forward: enhancing the hydrolysis rate of UiO-66 by decreasing [OH^-]. *ACS Catal.* **5**, 4637–4642 (2015).
36. Islamoglu, T. et al. Presence versus proximity: The role of pendant amines in the catalytic hydrolysis of a nerve agent simulant. *Angew. Chem. Int. Ed.* **57**, 1949–1953 (2018).
37. Troya, D. Reaction mechanism of nerve-agent decomposition with Zr-based metal organic frameworks. *J. Phys. Chem. C.* **120**, 29312–29323 (2016).
38. Chen, H., Liao, P., Mendonca, M. L. & Snurr, R. Q. Insights into catalytic hydrolysis of organophosphate warfare agents by metal–organic framework NU-1000. *J. Phys. Chem. C.* **122**, 12362–12368 (2018).
39. Mitoraj, M. P., Michalak, A. & Ziegler, T. A combined charge and energy decomposition scheme for bond analysis. *J. Chem. Theo. Comput.* **5**, 962–975 (2009).
40. Torbina, V., Ten, S. & Vodyankina, O. Effect of organic linker substituent on catalytic activity of UiO-66 metal-organic framework in selective oxidation of propylene glycol: homolytic versus heterolytic activation of hydrogen peroxide. *Mater. Today Chem.* **24**, 100776 (2022).
41. Zhang, G. & Musgrave, C. B. Comparison of DFT methods for molecular orbital eigenvalue calculations. *J. Phys. Chem. A* **111**, 1554–1561 (2007).
42. Wang, Y., Liang, Y., Bo, T., Meng, S. & Liu, M. Orbital dependence in single-atom electrocatalytic reactions. *J. Phys. Chem. Lett.* **13**, 5969–5976 (2022).
43. Baik, M.-H., Gherman, B. F., Friesner, R. A. & Lippard, S. J. Hydroxylation of methane by non-heme diiron enzymes: molecular orbital analysis of C−H bond activation by reactive intermediate Q. *J. Am. Chem. Soc.* **124**, 14608–14615 (2002).
44. Wu, X. P. & Gong, X. Q. Unique electronic and structural effects in vanadia/ceria-catalyzed reactions. *J. Am. Chem. Soc.* **137**, 13228–13231 (2015).
45. Lu, F. et al. Revealing the role of d orbitals of transition-metal-doped titanium oxide on high-efficient oxygen reduction. *CCS Chem.* **3**, 180–188 (2021).
46. Yang, D. et al. Tuning catalytic sites on Zr_6O_8 metal–organic framework nodes via ligand and defect chemistry probed with tert-butyl alcohol dehydration to isobutylene. *J. Am. Chem. Soc.* **142**, 8044–8056 (2020).
47. Al-Attas, T. A. et al. Ligand-engineered metal–organic frameworks for electrochemical reduction of carbon dioxide to carbon monoxide. *ACS Catal.* **11**, 7350–7357 (2021).
48. Vogiatzis, K. D. et al. Computational approach to molecular catalysis by 3d transition metals: challenges and opportunities. *Chem. Rev.* **119**, 2453–2523 (2019).
49. Yang, D. et al. Structure and dynamics of Zr_6O_8 metal-organic framework node surfaces probed with ethanol dehydration as a catalytic test reaction. *J. Am. Chem. Soc.* **140**, 3751–3759 (2018).
50. Odoh, S. O., Cramer, C. J., Truhlar, D. G. & Gagliardi, L. Quantum-chemical characterization of the properties and reactivities of metal–organic frameworks. *Chem. Rev.* **115**, 6051–6111 (2015).
51. Zhao, Y. & Truhlar, D. G. The M06 suite of density functionals for main group thermochemistry, thermochemical kinetics, noncovalent interactions, excited states, and transition elements: two new functionals and systematic testing of four M06-class functionals and 12 other functionals. *Theo. Chem. Acc.* **120**, 215–241 (2008).
52. Tomasi, J., Mennucci, B. & Cammi, R. Quantum mechanical continuum solvation models. *Chem. Rev.* **105**, 2999–3094 (2005).
53. Fukui, K. The path of chemical reactions - the IRC approach. *Acc. Chem. Res.* **14**, 363–368 (1981).
54. Schlegel, H. P. H. A. H. B. *Theory and applications of computational chemistry the first forty years*. 195-249 (Elsevier, Amsterdam, 2005).
55. Reed, A. E., Weinstock, R. B. & Weinhold, F. Natural population analysis. *J. Chem. Phys.* **83**, 735–746 (1985).
56. Hay, P. J. & Wadt, W. R. Ab initio effective core potentials for molecular calculations. Potentials for the transition metal atoms Sc to Hg. *J. Chem. Phys.* **82**, 270–283 (1985).
57. Rassolov, V. A., Ratner, M. A., Pople, J. A., Redfern, P. C. & Curtiss, L. A. 6-31G* basis set for third-row atoms. *J. Comput. Chem.* **22**, 976–984 (2001).
58. Gaussian 09, Revision D.01 (Gaussian, Inc., Wallingford CT., 2009).
59. Becke, A. D. Density-functional exchange-energy approximation with correct asymptotic behavior. *Phys. Rev. A* **38**, 3098–3100 (1988).
60. Perdew, J. P. Density-functional approximation for the correlation energy of the inhomogeneous electron gas. *Phys. Rev. B* **33**, 8822–8824 (1986).
61. Perdew, J. P. Erratum: density-functional approximation for the correlation energy of the inhomogeneous electron gas. *Phys. Rev. B* **34**, 7406–7406 (1986).
62. te Velde, G. et al. Chemistry with ADF. *J. Comput. Chem.* **22**, 931–967 (2001).
63. Gao, X. J. & Gao, X. Computational study on the mechanisms of multiple complexation of CO and isonitrile ligands to boron. *J. Phys. Chem. A* **121**, 2688–2697 (2017).

ACKNOWLEDGEMENTS

We thank Prof. Hui Wei at Nanjing University and Dr. Jiangjiexing Wu at Tianjin University for their helpful discussion. This work was supported by the National Natural Science Foundation of China (52161135107) and Program for International S&T Cooperation Projects of the Ministry of Science and Technology of China (2018YFE0117200).

AUTHOR CONTRIBUTIONS

X.G. conceived the project. X.J.G. performed the energy decomposition analysis. Z.W. performed all other calculations. H.M. and J.J.Z. advised on the results. Z.W. drafted the initial manuscript, then X.G. prepared the final manuscript with approval from all the authors.

COMPETING INTERESTS

The authors declare no competing interests.

ADDITIONAL INFORMATION

Supplementary information The online version contains supplementary material available at https://doi.org/10.1038/s41524-023-01008-5.

Correspondence and requests for materials should be addressed to Xingfa Gao.

Reprints and permission information is available at http://www.nature.com/reprints

Publisher's note Springer Nature remains neutral with regard to jurisdictional claims in published maps and institutional affiliations.